

Digital Differential Interference Contrast Autofocus for High-Resolution Oil-Immersion Microscopy

Feimo Shen,¹ Louis Hodgson,¹ Jeffrey H. Price,^{2,3*} Klaus M. Hahn^{1*}

¹Department of Pharmacology and Lineberger Cancer Center, University of North Carolina at Chapel Hill, Chapel Hill, North Carolina 27599

²Burnham Institute for Medical Research, La Jolla, CA 92037

³Vala Sciences Inc., San Diego, California 92121

Received 8 May 2007; Revision Received 6 January 2008; Accepted 18 February 2008

Grant sponsor: NIH; Grant numbers: GM64346, EB006200, HG003916.

*Correspondence to: Klaus M. Hahn, Department of Pharmacology and Lineberger Cancer Center, University of North Carolina at Chapel Hill, 1106 Mary Ellen Jones Bldg., CB#7365, Chapel Hill, NC 27599. or Jeffrey H. Price, Burnham Institute for Medical Research, 10901 N. Torrey Pines Rd., La Jolla, CA 92037 and Vala Sciences Inc., 9855 Towne Centre Drive, Suite 200, San Diego, CA 92121.

Email: khahn@med.unc.edu or jprice@burnham.org

Published online 7 April 2008 in Wiley InterScience (www.interscience.wiley.com)

DOI: 10.1002/cyto.a.20558

© 2008 International Society for Advancement of Cytometry

• Abstract

Continued advances in cellular fluorescent biosensors enable studying intracellular protein dynamics in individual, living cells. Autofocus is valuable in such studies to compensate for temperature drift, uneven substrate over multiple fields of view, and cell growth during long-term high-resolution time-lapse studies of hours to days. Observing cellular dynamics with the highest possible resolution and sensitivity motivates the use of high numerical aperture (NA) oil-immersion objectives, and control of fluorescence exposure to minimize phototoxicity. To limit phototoxicity, to maximize light throughput of the objective for biosensor studies, and because phase contrast is distorted by the meniscus in microtiter plates, we studied autofocus in differential interference contrast (DIC) microscopy with a 60× 1.45 NA oil objective after removing the analyzer from the fluorescent light path. Based on a study of the experimental DIC modulation transfer function, we designed a new bandpass digital filter for measuring image sharpness. Repeated tests of DIC autofocus with this digital filter on 225 fields-of-view resulted in a precision of 8.6 nm (standard deviation). Autofocus trials on specimens with thicknesses from 9.47 to 33.20 μm, controlled by cell plating density, showed that autofocus precision was independent of specimen thickness. The results demonstrated that the selected spatial frequencies enabled very high-precision autofocus for high NA DIC automated microscopy, thereby potentially removing the problems of meniscus distortion in phase contrast imaging of microtiter plates and rendering the toxicity of additional fluorescence exposure unnecessary. © 2008 International Society for Advancement of Cytometry

• Key terms

autofocus; image cytometry; lab automation; differential interference contrast; modulation transfer function

IMAGE cytometry enables multidimensional measurements on cell populations during studies in chemical genomics and intervention by drugs, RNAs, and cDNAs. Obtaining an in-depth understanding of the heterogeneous responses across cell populations in these studies has motivated high-resolution time-lapse measurements of subcellular dynamics in living cells (1). Heterogeneity even in clonal cell culture populations motivates scanning multiple fields of view (FOVs), while heterogeneity is even greater in other populations, e.g., differentiating embryonic stem cell colonies. High-resolution, time-lapse image acquisition on multiple FOVs requires high-precision autofocus (small depths of field) with immersion objectives.

The challenge of designing high-performance autofocus increases as the depth of field shrinks proportionally with numerical aperture (NA²). The smaller depths of field make it increasingly difficult to maintain focus during time-lapse image acquisition as objective NA is increased. The challenge is compounded in extended time-lapse studies, where cell growth, ambient temperature fluctuations, and other microscope instabilities have in some cases necessitated manual focusing over hours to enable time-lapse imaging. Interesting events which take place over longer time scales (i.e., cell division and differentiation) motivate development of robust automation.

The goal of resolving minute ultrastructural details drives use of the highest NA objectives available. Studying these details in living cells undergoing phenotypic changes motivates minimizing light exposure, which is much more damaging with fluorescence imaging than during transmitted light microscopy. Finally, fluorescent biosensors that reveal the sub-cellular dynamics of protein activity are frequently limited by the light-gathering capacity of the microscope and by photobleaching (2–5). For these reasons, we designed and verified a new high-performance autofocus technique for high-resolution oil-immersion microscopy, using transmitted light differential interference contrast (DIC) imaging rather than fluorescence imaging. We used bright field rather than fluorescence to minimize the phototoxicity. For the new studies reported here, we wished to explore DIC for autofocus to: 1) avoid the problem of the meniscus distorting phase contrast in microtiter wells (96-well glass bottom), 2) prevent the loss of fluorescence emission light caused by the objective phase ring, and 3) take advantage the higher spatial resolution (i.e., high-pass filter characteristics) of DIC when compared with phase contrast (6).

Microscopy autofocus was implemented as early as the 1970s (7–9). This was followed by a pivotal comparison of microscopy autofocus methods on single FOVs in 1985 (10), upon which we built our extended comparison of the performance of autofocus algorithms, using phase contrast and fluorescence microscopy on thousands of FOVs (11). We refer the reader to these two papers for more extensive tutorials and a larger set of references to the autofocus literature. These comparison studies led to a theoretical understanding of autofocus, in which image sharpness is measured using a highpass/bandpass filter that isolates high spatial frequencies (12). We implemented these focus measurement techniques in a circuit, and tested their performance on thousands of FOVs in phase contrast, demonstrating precision of better than 100 nm for a 20× 0.75 NA objective with a Rayleigh depth of field of 740 nm at a wavelength of 500 nm (13).

Optical characteristics, including resolution, are described by the modulation transfer function (MTF) of the imaging system, which exhibits a unique set of characteristics for each mode of contrast generation. The MTFs are different for DIC, phase-contrast, and bright field (6). Our goal was to enable a combination of high autofocus performance and efficient light gathering for fluorescence emission at the highest resolutions. To maximize autofocus performance for the DIC MTF, we designed a new bandpass finite impulse response (FIR) filter to select the appropriate spatial frequency band with the best signal-to-noise ratio (SNR) and smallest distorting side peaks. Side peaks result from contrast reversals and were observed to increase when additional lower frequencies were included in the passband for phase and bright field (11,12). This makes focus measurement filter design a tradeoff between creating a sharp unimodal peak by including only the highest frequencies (and lowest SNRs), and increasing the SNR by including lower frequencies. The latter decreases the sharpness of the focus measurement maximum, thereby decreasing precision, and causing side peaks. The appropriate

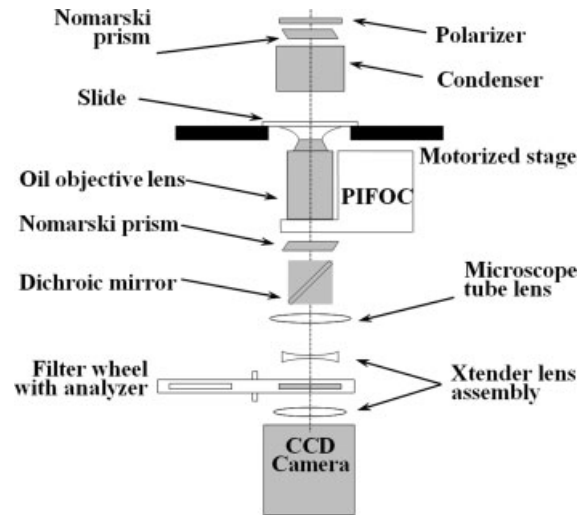


Figure 1. A schematic of the microscope autofocus module is shown. This setup is based on an inverted microscope. The camera is mounted on the bottom port of the microscope directly underneath the objective lens. An Xtender is used to create an infinity space for the filter wheel so that the optics in the filter wheel have no optical effect and do not degrade image formation at the CCD.

tradeoffs were made to design a new bandpass filter that was then tested with an oil-immersion DIC objective and customized optics in repeated autofocus trials.

MATERIALS AND METHODS

Hardware

A digital autofocus module was designed and built on a microscope-based image cytometer (inverted, Olympus model IX71, Olympus America, Melville, NY). Figure 1 shows a schematic diagram of the setup. The microscope was equipped with DIC optics. DIC imaging performs with an optical high-pass filter analogous to phase contrast, but with a higher resolution cutoff for higher autofocus precision. By removing the analyzer from the fluorescence light path, we expected to achieve improved autofocus performance via the increased contrast and higher frequency characteristics of DIC without losing significant fluorescence light transmission. The remaining DIC prism decreased the fluorescence intensity by 1.18% (as measured by comparing the averages of 10 fluorescence images acquired with and without the prism). Since this light loss was small and the image quality appeared identical with and without the prism, we left it in place at the back of the objective to retain the best possible DIC imaging performance. The benefits of DIC or phase contrast are most important with the highest resolution optics where bright field contrast is lowest (6). Although phase-contrast imaging produces excellent contrast, phase objective lenses have a high optical density phase plate in the back focal plane that blocks some of the fluorescent light. In addition, the small well in a microtiter plate (density ≥ 96 wells) has a meniscus that laterally shifts (by an amount dependent on the distance from the center of

the meniscus) and magnifies the image of the condenser phase ring in the back focal plane (effects visualized directly by using the Bertrand lens or phase telescope). This severely compromises image contrast. These considerations were expected to make DIC the best choice for high-resolution autofocus.

For computerized focusing, we positioned the objective lens in the axial, or z -direction, with a piezoelectric transducer between the objective turret of the microscope and the objective lens. This micropositioner, a Physik Instrumente P/N 7-721.10 PIFOC (Auburn, MA) with a linear variable displacement transducer for negative feedback controlled positioning, had a travel range of 100 μm and an analog precision of 25 nm (or about that of a 12-bit D/A converter). The PIFOC was connected to an E-662 LVPZT amplifier with built-in servo feedback control. The objective was a 60 \times oil 1.45 NA PlanApo DIC TIRF objective (Olympus America). The axial displacement of the objective from the Nomarski prism by the PIFOC introduced intensity shading across the DIC image.

A motorized stage (P/N 99S108-02, Ludl Electronic Products, Hawthorne, NY) was used to translate the specimen in the x - y plane for scanning. The stage had a linear encoder with 100-nm resolution for each axis. The optional piezoelectric transducer stage insert for vertical specimen positioning was unavailable to us, but would eliminate the DIC shade distortion caused by the PIFOC. The stage motors were driven by a National Instruments MID-7604 power drive (National Instruments, Austin, TX) and were interfaced to the control computer using a PCI-7358 board (National Instruments). The same board also performed 16-bit D/A conversion (which had higher precision than expected from the PIFOC) to control the piezo device by outputting a 0.0–10.0 V direct current (DC) voltage. The computer was a Pentium Xeon dual 2.4-GHz CPU computer (model Precision 650, Dell, Round Rock, TX) and it was programmed to automatically control the motion of the stage and piezo device, acquire the images, and compute the autofocus functions.

A 12-bit monochrome scientific-grade digital Photometrics CoolSNAP ES camera (with $1,392 \times 1,040$, $6.45 \times 6.45 \mu\text{m}^2$ CCD pixels) was interfaced via a PVCAM PCI card (both from Roper Scientific, Tucson, AZ) with the computer to capture images for autofocus. This combination performed fast region-of-interest (ROI) acquisition for focusing on a specified central 600×600 pixel region in the FOV. A DC motor filter wheel (P/N 99A305, Ludl Electronic Products) was mounted outside of the microscope, below the bottom port, in the infinity optical space between the two parts of an Xtender (Optical Insights, Tucson, AZ). The 10-position filter wheel contained an antireflection-coated linear polarizer for DIC imaging that was automatically replaced with the proper fluorescence emission filter after autofocusing. The same filter wheel can switch a blank position into the optical path to achieve bright-field imaging. When needed, DIC, fluorescence, and bright-field imaging can be achieved sequentially in any order by programming the filter wheel controls. The bottom port of the microscope was used to capture the image so that light loss and image distortion were minimized. Figure 1 shows the setup as a side-view of the microscope. This setup is

adaptable to any microscope, pending availability of adaptors for different kinds of camera mounts.

Software and Autofocus Implementation

The software carried out the autofocus calculation instructions and was written in Visual C++ (version .NET 2003, Microsoft Corp, Redmond, WA). Resolution decreases when an image was defocused. The autofocus method was based on setting the focus to the axial position that maximized a measure of the power of a one-dimensional (horizontal video lines) band of high spatial frequencies (or sharpness). Loss of resolution is manifested by a decrease in the high spatial frequencies of the images as they become more out-of-focus. The focus measurement routine measured the high-frequency content at several planes for each FOV. High frequencies were selected from the full frequency spectrum of the image by applying a bandpass filter. The C/C++ Intel Image Processing Library v2.5 (Intel, Santa Clara, CA) was used to perform the convolution filter and other calculations.

The function used to compute the focus index for an image was

$$F(z) = \frac{\sum_x \sum_y [f(x, y) \otimes i_z(x, y)]^2}{\left[\sum_x \sum_y i_z(x, y) \right]^2}, \quad (1)$$

where (x, y) is the discrete coordinate in the image, and $i_z(x, y)$ is the image acquired at each focus position, z . \otimes stands for the convolution operator and $f(x, y)$ is a high-pass or band-pass filter (11). Here, we use a 1-D filter, $f(x, y) = f(x)$. The denominator, which is squared to match the power of the numerator, normalizes variations in illumination. Best focus, B , was computed from a set of focus indices, $F(z)$, by the power-weighted average.

$$B = \frac{\sum z F(z)^m}{\sum F(z)^m}, \quad (2)$$

where $m = 12$ (11). If m is very large, Eq. (2) returns the position with the maximum sharpness and if $m = 1.0$, the value returned is the sharpness-weighted-average of the axial positions tested. With intermediate values the maximum dominates, but averaging also influences the result especially when there are nearly equal maxima near best focus, which often occurs when specimen is thicker than the depth of field of the optics. This function performed better (resulted in higher measured precision and better observed accuracy) in our hands than smoothing and curve fitting.

To summarize, scanning was carried out as follows: 1) the specimen was placed on the stage, the microscope was aligned, the scanning area was defined, the stage was moved to the first field, and the microscope was placed near best focus manually; 2) a focus measurement sequence was carried by moving the objective with the PIFOC through a prescribed series of z -steps to acquire an image at each axial position; 3) Eq. (1) was applied to each image to produce a focus measurement at

each axial position; 4) Eq. (2) was applied to the series of focus measurements to calculate the best focus; 5) the PIFOC was set to the best focus position and the image acquired (for fluorescence, the arc lamp shutter was then opened, the filter wheels positioned to acquire the appropriate channel, the image was acquired, and the shutter was closed); 6) the stage was moved laterally to the next position and the steps were repeated until the area was scanned; and 7) for time-lapse imaging, the entire sequence would be repeated (without manual focusing at the start of the area) as many times as needed.

Experimental Autofocus Design

Sampling. The spatial frequency cutoff is (14)

$$f_c = (NA_{\text{obj}} + NA_{\text{cond}})/\lambda \quad (3)$$

With the TIRF 60× 1.45 NA objective lens, the 0.55 NA condenser lens, $\lambda = 420$ nm (broad bandpass filter, with 50% transmittance at 355 and 475 nm), $NA_{\text{obj}} = 1.45$ and $NA_{\text{cond}} = 0.55$, Eq. (3) gives $f_c = 4.762 \mu\text{m}^{-1}$ and resolution $d = 1/f_c = 0.210 \mu\text{m}$. Note that we used the cutoff criterion, which provides a higher resolution estimate than the Rayleigh criterion, because resolution is dependent on the SNR, and measuring sharpness using all of the pixels in the image provides a very high SNR. Nyquist sampling is double the spatial frequency or $d/2 = 0.105 \mu\text{m}$. This magnification and CCD pixel size resulted in $0.107 \mu\text{m}/\text{pixel}$ sampling, which is $0.981\times$ vs. Nyquist of the cutoff criterion, or slightly theoretically undersampled. The experimental cutoff spatial frequency is demonstrated in the 1-D through-focus power spectra plotted in Figure 2. For clarity, the DC components of the spectra were removed by subtracting the mean intensity of the image from each pixel. For both panels [that of a micrometer (b) and of a cell lamellipodium (d)] in Figure 2, the upper bound of the normalized frequency (see arrows) has signal above the noise floor. Therefore, the experimental cutoff frequency is outside of the normalized frequency domain (i.e., >0.5). Thus, this demonstrates undersampling experimentally, despite the use of the more conservative cutoff criterion to predict the maximum resolution.

Filter design. The digital filter for autofocus was designed to pass a suitable spatial frequency band. The through-focus spatial frequency information can be summarized by the power spectra as shown in Figure 2. Simple integer filters (10,11) such as the 1-D derivative filter $[-1 \ 0 \ 1]$ have a broader band that passes much more of the medium and low frequencies than specialized, custom-designed filters such as the 31-tap floating-point kernel we designed previously (12). Inspection of the through-focus power spectra in Figure 2 reveals contrast reversals in the micrometer spectra of panel (a) but not in the cell spectra of panel (c). As previously described, thicker specimens (relative to the depth of field) average out contrast reversals (12) and this may be the reason for the smoother spectra in panel (c). Even the micrometer spectra exhibit less contrast

reversals than we saw with a 40× 0.85 NA phase contrast objective in our earlier study (12). Both the higher NA of the objective and the smaller depths of field inherent in polarization/DIC microscopy (6) may act to average out the contrast reversals and decrease the specimen depths at which side peaks disappear. That is, the probability of side peaks decreases with higher NA and with DIC because the depths of field are narrower relative to the thicknesses of the tissue specimens. The spectrum in Figure 2c was created from the image of a cell selected because of its large lamellipodial sheet, which is the thinnest part of a cell (Fig. 2d). This very thin specimen was selected with the intention of testing the greatest contrast reversals possible in the cell specimens which we wish to image. Since contrast reversals were not observed, we were able to increase the SNR more by including lower spatial frequencies in the passband of the sharpness measurement filter. To design a filter that maximized the dynamic range without creating side peaks, we further studied the frequency spectra as shown in Figure 3. In Figure 3a, the normalized spectra are plotted for the axial position ($0 \mu\text{m}$) in Figure 2c. This position gave the maximum (max, labeled solid black) and minimum (min, labeled dashed black) powers near the middle frequencies where the height of the unimodal ridge is greatest relative to the floor of the spectrum. These spectra allow us to choose the best frequency band to use for analyzing sharpness of the image. To find the range of these middle frequencies more easily, a third trace in Figure 3a is plotted to show the normalized ratio of the two, maximum/minimum (max/min, labeled solid gray); the frequencies at which max/min is greatest were expected to provide the highest dynamic range for focus measurement. This dynamic range (in the solid gray trace) peaks between 0.1 and 0.2 in the normalized frequency domain. Based on this observation, a one-dimensional, 31-tap FIR filter was designed to pass a normalized frequency band between 0.12 and 0.2 with its peak centered at 0.16. For this we used the MATLAB (Mathworks, Natick, MA) function FIR2 filter design tool. The filter spectrum is shown in Figure 3b in comparison with filter $[-1 \ 0 \ 1]$ and Oliva's filter. The coefficients of the new filter are $[0.001419, -6.5805 \text{ e } -005, -0.0005887, 0.00087719, 0.00033475, -0.0087167, -0.019188, -0.0066311, 0.036884, 0.068512, 0.028805, -0.071599, -0.13087, -0.062856, 0.083878, 0.16016, 0.083878, -0.062856, -0.13087, -0.071599, 0.028805, 0.068512, 0.036884, -0.0066311, -0.019188, -0.0087167, 0.00033475, 0.00087719, -0.0005887, -6.5805 \text{ e } -005, 0.001419]$. This digital filter was used in the following experiments.

Oil-Immersion Viscosity and Autofocus Speed

With oil- or water-immersion objectives, axial positioning had to be slower than that of air-immersion objectives, because of the viscosity of the immersion medium. If the objective lens is moved too quickly toward the specimen, the immersion medium moves the specimen because the high viscosity prevents it from flowing away fast enough. Because the medium is incompressible, either the specimen is pushed away

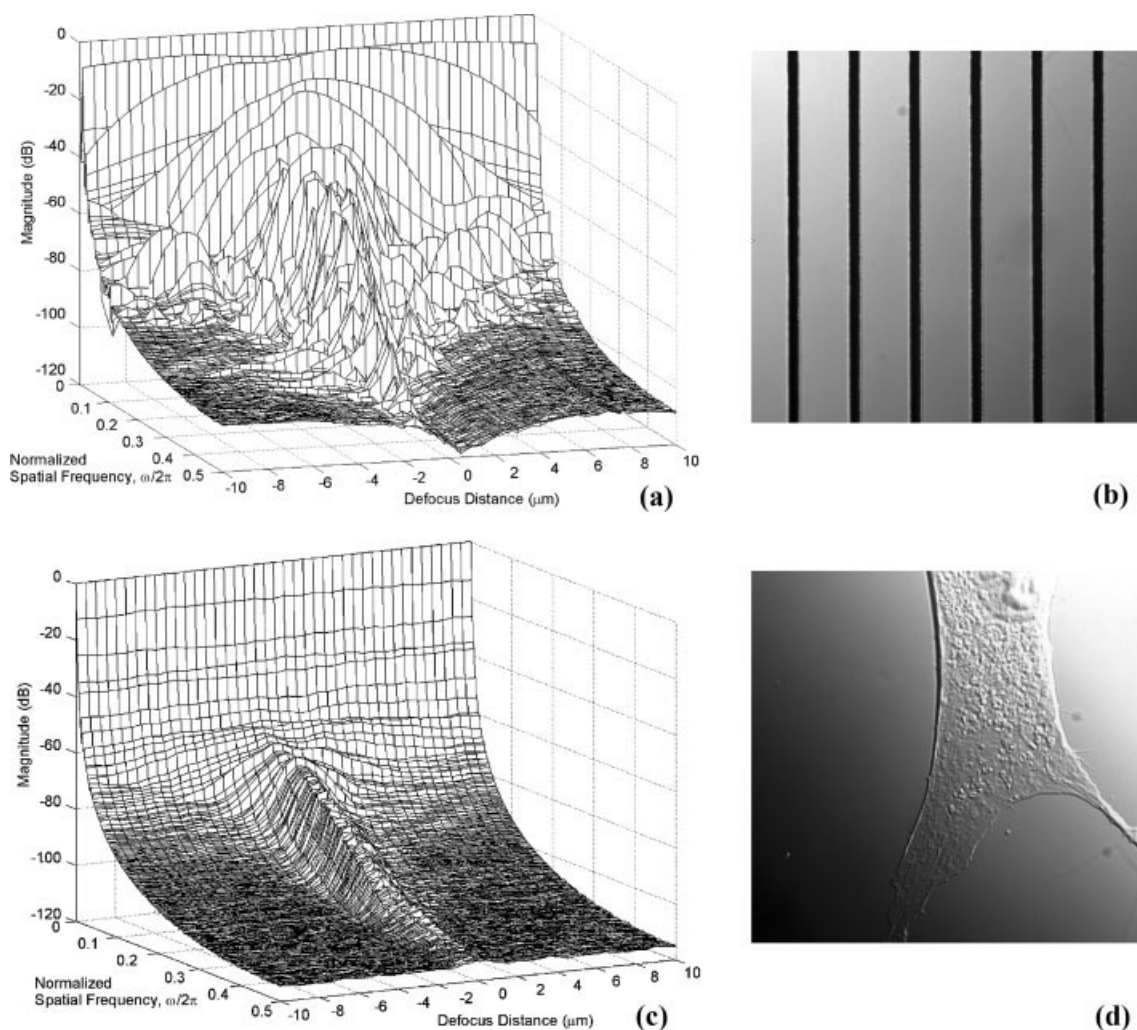
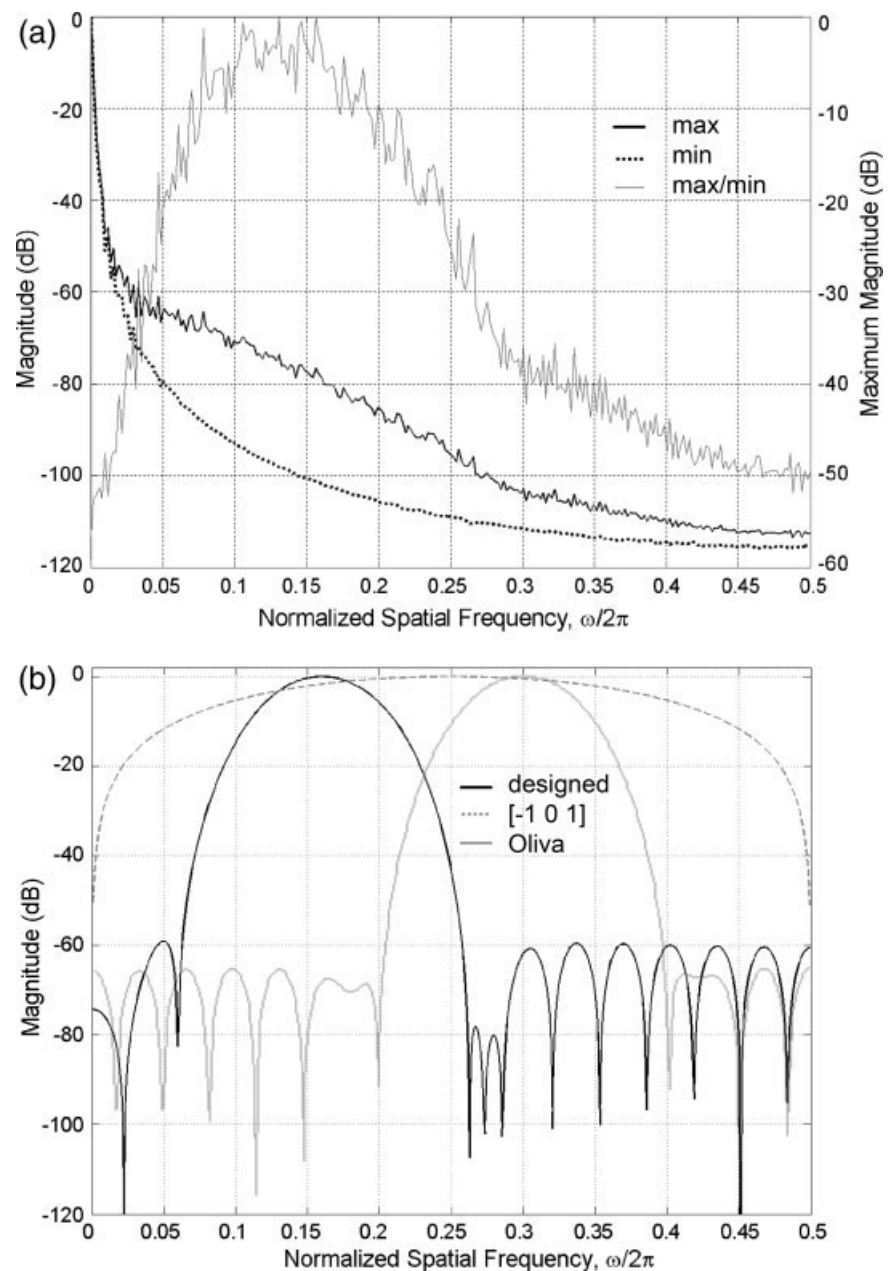


Figure 2. The top row shows a through-focus power spectrum (a) of a Zeiss stage micrometer. (b) The bottom row shows a through-focus power spectrum (c) of a fixed fibroblast lamellipodium (d). Optical sections were acquired at $0.50\text{-}\mu\text{m}$ axial steps to create a z-stack for each specimen, from which the power spectra were computed. For clarity, the DC components of the spectra were removed by subtracting the mean image intensity from each pixel prior to taking the 1-D Fourier transform of each horizontal (x direction) line. The 1-D spectrum for each axial position was then computed after averaging across all lines in Fourier space. This is the best way to model the tremendous gain in the focus measurement SNR because of using the entire image. Conceptually, the highest spatial frequencies represent the sharpest/finest image components and, as with all optical systems, the strength (magnitude) of them is lowest. The side peaks in (a) are due to the contrast reversals [see the Airy pattern and spoke patterns in Figs. 2–18 and 2–25 of Inou and Spring (6)] that change as a function of defocus [see also Born and Wolf (15), Fig. 8.41 for an example of the 3-D intensity contour lines]. The focus function curves in Figure 5 were computed on these same z-stacks. The $10\text{-}\mu\text{m}$ -spaced lines in the micrometer image provide the scale for both (c) and (d).

from the objective, or the spring mechanism near the objective face is pushed away from the specimen. The specimen and the objective spring are elastic and yield as the medium flows to the sides, so the system reaches a new state of equilibrium. To compensate, the axial positioning and the image acquisition must be delayed appropriately after the PIFOC is repositioned for each sharpness measurement. To systematically determine the appropriate delay, we studied the relationship between autofocus precision as a function of the delay. To further speed autofocus, we studied the precision with oils of two different viscosities—5600 cSt and 150 cSt (Cargill oil, Canemco-Mari- vac, Lakefield, Quebec, Canada).

In this experiment, we varied the delay time between PIFOC axial repositioning and image acquisition for autofocus with the two different immersion oils. Standard deviation (SD) of the output of the best focus positions were used to measure autofocus precision. Figure 4 demonstrates the trends of increasing focus precision (lower SDs) as functions of longer delay times for both viscosities. The 5600 cSt oil had not yet reached a plateau at a delay of 70 ms, whereas the 150 cSt oil began to plateau at about 15 ms, demonstrating a dramatic advantage for low-viscosity oils. This experiment led to selection of the lowest viscosity immersion oil we found, which is Olympus immersion oil (Olympus America) with a viscosity

Figure 3. (a) Normalized spectra are shown for the axial positions in Figure 2b which gave the maximum (max, solid black) and minimum (min, dotted black) powers near the middle frequencies (0.1–0.2 in the normalized frequency domain) where the height of the unimodal ridge is greatest relative to the floor of the spectrum. The third trace is the normalized ratio maximum/minimum (max/min, solid gray) which provides the basis for filter design to capture the peak. (b) The magnitude of the 31-tap filter designed to capture the peak of the max/min plot at $0 \mu\text{m}$ in the axial position in (a) (solid black) compared with filter $[-1 \ 0 \ 1]$ (dashed gray), which demonstrates a much broader passband. The Oliva FIR filter is present in solid gray for further comparison. The bottom figure aligns with the top figure in the frequency axis (abscissa). The designed filter (solid black) has a passing band between 0.1 and 0.2 in the normalized frequency domain.



of 135 cSt at 23°C . This oil does not autofluoresce, whereas Cargill oils did. The index of refraction of this oil is 1.516 and thus matches the BK7 glass normally used for cover glasses. This oil was used with a conservative delay of 50 ms to ensure that the focus position had completely settled. With sampling at every 500 nm in the z direction through a $2\text{-}\mu\text{m}$ focus range, autofocus can be completed in <1.0 s.

RESULTS

Autofocus was tested using a newly designed DIC-specific FIR filter on two different types of specimens, a micrometer and a cell with a large lamellipodium (Fig. 2). The filter is shown as a solid black curve in the normalized frequency

domain in Figure 3b, where it is compared with a simple $[-1 \ 0 \ 1]$ filter and the FIR filter previously designed for the $40\times$ 0.85 NA objective lens in phase-contrast (12). An axial range of $20 \mu\text{m}$ was sampled in 41 equally spaced steps of $0.50 \mu\text{m}$ to plot the focus function curves (Fig. 5). A range much larger than that necessary for autofocus was used, to completely characterize the focus measurement function. Consistent with the power spectra shown in Figure 2, the new filter produced a contrast reversal side peak in the focus function curve for the micrometer specimen (Fig. 5b). However, no contrast reversal side peak was generated for the cell specimen (Fig. 5d). There were no contrast reversal side peaks generated for either specimen by Oliva's filter (Figs. 5a and 5c) as a result of the higher

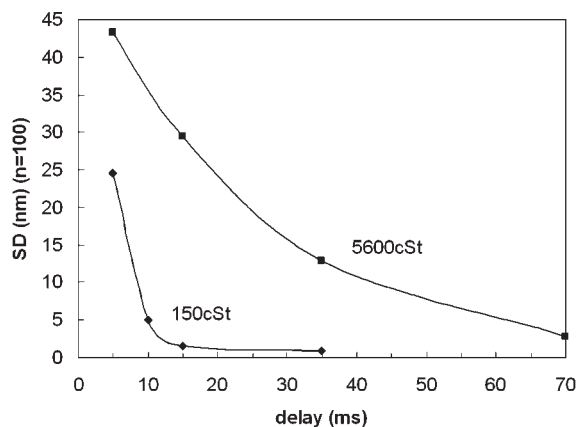


Figure 4. The standard deviation (SD) is used as a measure of precision of autofocus. It is shown as a function of the delay time for two different viscosity immersion oils, demonstrating that autofocus speed can be increased by lowering the oil viscosity.

frequency passband, but our new filter produced greater dynamic range, which should improve performance on specimens with low image content. For the micrometer, Oliva’s

filter produced a full-width half-maximum of $0.8 \mu\text{m}$, compared with $1.5 \mu\text{m}$ for the DIC-specific filter. For the cell specimen, the Oliva et al. filter produced a full-width half-maximum of $1.6 \mu\text{m}$ compared with $1.75 \mu\text{m}$ for the DIC-specific filter. Thus, the higher passband of the Oliva et al. filter produced narrower focus function curves. These focus function widths are also a function of the thicknesses of the specimens. The observation that there is little difference in the full-width-half maxima for the cell indicates that the cell is likely thicker than the depth of field, whereas the larger difference in full-width half-maximum for the micrometer likely indicates that it is thinner than the depth of field. The best focus positions of the Oliva et al. and new FIR filters on the micrometer specimen were 9.8 and $10.1 \mu\text{m}$, respectively, and on the cell specimen they were both $9.0 \mu\text{m}$, respectively. These differences are not meaningful, because they are within the $0.500 \mu\text{m}$ step size of the experiment. This is particularly evident in the cell image focus function curves; the peaks of both are likely blunted as a result of not sampling more finely in the axial direction. Another possible source of differences in best focus for the cell is the dependence of the powers of different frequencies on axial position; the highest power ridge shifts toward positive

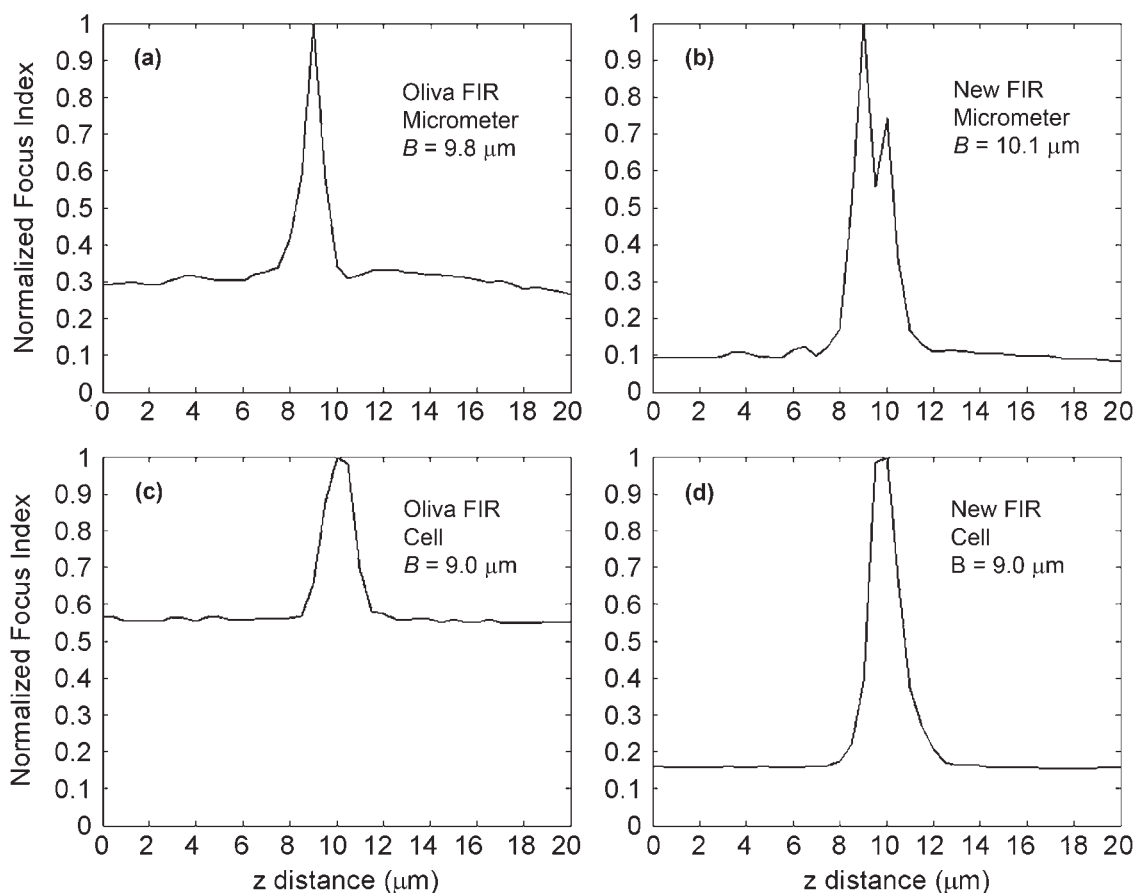


Figure 5. A comparison of focus function curves is shown. The new filter is compared with the Oliva filter, which was designed for phase-contrast air objective lenses (12). These focus function curves were obtained from the same specimens: top row, micrometer; bottom row, cell. B is the best focus position in microns. (a) Oliva 1999 filter micrometer image. (b) New DIC filter micrometer image. (c) Oliva 1999 filter cell image. (d) New DIC filter cell image.

Table 1. Standard deviations of autofocus trials with HEK 293 cells

PLATING DENSITY (MILLION CELLS/ML)	CELL THICKNESS (μM)	AUTOFOCUS SD (μM)	NUMBER OF FOV
0.5	9.47	0.0255	3
1	12.67	0.0214	3
2	14.00	0.0143	3
4	19.33	0.0340	3
8	22.80	0.0220	12
16	33.20	0.0129	12

defocus distance as the frequency increases (see Fig. 2c). This shift is likely due to the differences in image content at different focal planes in the biological image (micrometer lines would not be expected to show such a difference).

To test autofocus precision with the new system, 225 FOVs were randomly selected from a fixed specimen (3.7% formaldehyde) of mouse embryonic fibroblasts grown on a no. 1.5 cover glass (24.5 mm diameter, Lucas-Highland, Chantilly, VA), which was mounted in phosphate-buffered saline (Sigma-Aldrich Corp, St. Louis, MO) on a $75 \times 25 \text{ mm}^2$ plain glass slide (Cat. no. 12-550A, Fisher Scientific, Pittsburgh, PA). These FOVs represented a wide range of image content to test the variety of conditions expected in scans of large numbers of fields. The images included fields with no whole cells (only cellular debris), single cells, and clumps of overlapping cells. To determine the best focus positions for these FOVs, 21 axial planes, each 100 nm apart, were imaged in a $2.0\text{-}\mu\text{m}$ focus range for each FOV. A 50-ms delay between PIFO movement and image acquisition ensured that the target

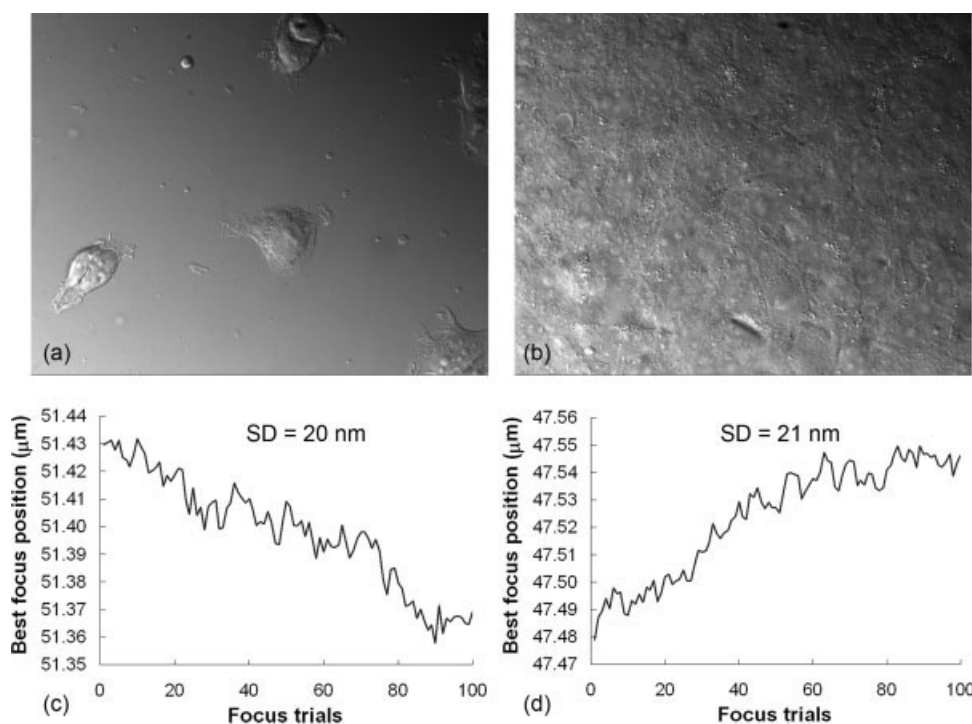
positions were reached. For each FOV, autofocus was calculated 50 consecutive times using Eqs. (1) and (2) and the SD was calculated as a measure of precision. Over the 225 regions, the SD of optimal focus positions ranged from a minimum of 2.2 nm to a maximum of 34.4 nm with a mean ($n = 225$) of 8.6 nm. ROIs with large, thin cellular lamellipodia gave smaller SDs, whereas overlapping clumps and contracted, thick cells created larger SDs. The combined SD is given as

$$\text{SD}_{\text{comb}} = \sqrt{\frac{1}{n} \sum \sigma_n^2}, \quad (4)$$

where σ is the SD at each FOV, n , for all 225 FOVs (and $225 \times 50 = 11,250$ autofocus trials) was 10.3 nm. This compares with a previous combined precision of 56 nm for a 20×0.75 NA phase contrast objective (13). This dramatic improvement is likely due to the much narrower depth of field of DIC vs. phase and NA 1.45 vs. NA 0.75.

To further study the dependence of autofocus performance on specimen thickness, human embryonic kidney (HEK 293) cells were grown on no. 1.5 glass cover glasses with different seeding densities. The densities varied from 0.5 to 8 million cells/ml. The cell thickness was a function of cell-plating density. To measure the thickness, the cells were stained with phalloidin tagged with Alexa-488 (Invitrogen, Carlsbad, CA). Cell thicknesses were then determined using a disk scanning unit confocal microscope (Olympus model IX71, Olympus America). The cover glasses were mounted and scanned with a setup identical to the previous scan shown above, except that autofocus was calculated 100 consecutive times. A total of 36 FOVs and $36 \times 100 = 3,600$ autofocus trials were performed.

Figure 6. Flat, isolated cells versus thick, confluent cells is focused. (a) The isolated, thin cells were measured by confocal microscopy to have a thickness of 9.47 μm (plated at 0.5 million cells per ml). (b) The confluent specimen had a thickness of 33.20 μm when plated at 16 million cells per ml. (c) Best focus positions for the 100 consecutive autofocus trials of the FOV in (a). (d) Best focus positions for the 100 consecutive autofocus trials of the FOV in (b).



The SDs of these autofocus trials are summarized in Table 1. The data show that, as the cell-plating density increases, the cell thickness increases monotonically ($r^2 = 0.97$). However, there is no trend for the SD of the autofocus results ($r^2 = 0.28$). The autofocus SDs vary from 0.013 for 33.20- μm -thick cells to 0.034 μm for 19.33- μm -thick cells. Two example fields are shown in Figures 6a and 6b for the thinnest and thickest cells scanned in this experiment. The corresponding output of autofocus positions over the 100 trials are shown in Figures 6c and 6d. The abscissa is focus trials carried out sequentially so that it also represents time. It is interesting to note that best foci plots appear to have both random and baseline (drift) components. The slower drift components over time could be due to temperature or other mechanical drift, but this was not tested. The reason that the precision is largely independent of specimen thickness and better than the z -step size is that the best focus position is a power-weighted average of all of the focus measurements [see Eq. (2)].

DISCUSSION AND CONCLUSIONS

Neither water nor oil immersion objectives are designed to match the varying indices of refraction of biological specimens, which lie in between the design parameters of the two. The full resolution of high-NA oil-immersion objectives cannot be achieved with cells attached to the other side of a cover glass. The index of refraction of cytoplasm ranges from 1.358 to 1.374 (14), and that of lipid is ~ 1.48 (16). While greater than water, these indices are below the 1.515 index of refraction of the cover glass and the matching immersion oil. Thus, the critical angle prevents the highest angle light from filling the NA to achieve maximum resolution. Oil immersion was used instead of water for this study because it was thought that the higher NA may perform better on thin cells attached directly to the cover glass. We think that water immersion may perform better on thick specimens and oil immersion better on thin specimens. Both, however, are subject to aberrations caused by the index of refraction mismatch with the biological sample. The principles of our approach should also be directly applicable to filter design and autofocus implementation with a high NA water immersion DIC objective, which would also have the advantage of lower viscosity.

Our preliminary autofocus experiments on cover glass-bottom 96-well plates (Nunc Cat no. 265301, Nalge Nunc, Rochester, NY) worked effectively for subregions of 8×4 wells (data not shown). Routine automatic scanning of larger areas (e.g., for large-scale robotic screening) may require an oil retaining or reapplying system such as the refilling system for water immersion scanning on the PerkinElmer/Evotec Opera (Waltham, MA).

These results demonstrate high-performance DIC autofocus enabled by an FIR filter designed for cells attached to a cover glass for high-resolution microscopy experiments. The new filter was designed to provide the highest dynamic range for the thinnest cell specimen observed in our cell monolayers. Since side peaks generated by contrast-reversal were not observed, we were able to maximize dynamic range in the filter design. The effect of the viscosity of oil immersion was mitigated by using low-viscosity oil that enabled decreasing the delay between PIFOC positioning and image acquisition, which enabled oil-immersion autofocus speed of less than 1.0 s (with 500 nm sampling in the z direction through 2- μm focus range). From a scan of 225 fixed cell samples, autofocus precision was 10.3 nm, which was probably more than an order of magnitude better than the DIC depth of field. In an experiment that systematically varied cell thickness by changing the cell plating density, autofocus precision was independent of specimen thickness. This excellent performance will enable stable focus for high-resolution time-lapse studies of living cells in culture on the microscope stage for extended periods of time.

ACKNOWLEDGMENT

The authors thank Dr. Miguel Bravo-Zanoguera for his valuable advice.

LITERATURE CITED

- Shen F, Hodgson L, Rabinovich A, Pertz O, Hahn K, Price JH. Functional proteomics for cell migration. *Cytometry Part A* 2006;69A:563–572.
- Gaits F, Hahn K. Shedding light on cell signaling: Interpretation of FRET biosensors. *Sci STKE* 2003;165:3.
- Pertz O, Hodgson L, Klemke R, Hahn KM. Spatio-temporal dynamics of RhoA activity in migrating cells. *Nature* 2006;440:1069–1072.
- Nalbant P, Hodgson L, Kravnov V, Touthkine A, Hahn KM. Activation of endogenous Cdc42 visualized in living cells. *Science* 2004;305:1615–1619.
- Lalonde S, Ehrhardt DW, Frommer WB. Shining light on signaling and metabolic networks by genetically encoded biosensors. *Curr Opin Plant Biol* 2005;6:574–581.
- Inoue S, Spring KR. *Video Microscopy, The Fundamentals*, 2nd ed. New York: Plenum; 1997.584 p.
- Ingram M, Preston K Jr. Automated analysis of blood cells. *Sci Am* 1970;223:72–82.
- Mason DC, Green DK. Automatic focusing of a computer controlled microscope. *IEEE Trans Biomed Eng BME* 1975;22:312–317.
- Jarvis RA. Focus optimization criteria for computer image processing. *Microscope* 1976;24:163–171.
- Groen FC, Young IT, Ligthart G. A comparison of different focus functions for use in autofocus algorithms. *Cytometry* 1985;6:81–91.
- Price JH, Gough DA. Comparison of phase-contrast and fluorescence digital autofocus for scanning microscopy. *Cytometry* 1994;16:283–297.
- Oliva MA, Bravo-Zanoguera M, Price J. Filtering out contrast reversals for microscopy autofocus. *Appl Opt* 1999;38:638–646.
- Bravo-Zanoguera M, Massenbach B, Kellner A, Price J. High-performance autofocus circuit for biological microscopy. *Rev Sci Instrum* 1998;69:3966–3977.
- Lanni F, Waggoner A, Taylor D. Internal reflection fluorescence microscopy. *J Cell Biol* 1985;100:1091.
- Born M, Wolf E. *Principles of Optics*, 6th ed. Oxford: Pergamon; 1980.
- Beuthan J, Minet O, Helfman J, Muller G. The spatial variation of the refractive index in biological cells. *Phys Med Biol* 1996;41:369–382.